Journal of Magnetism and Magnetic Materials 432 (2017) 410–417

Contents lists available at ScienceDirect

Journal of Magnetism and Magnetic Materials

journal homepage: www.elsevier.com/locate/jmmm

Morphological and magnetic properties of sol-gel synthetized meso and macroporous spheres of barium hexaferrite ($BaFe_{12}O_{19}$)

S. Torres-Cadenas [a], José Reyes-Gasga [b,*], A. Bravo-Patiño [c], I. Betancourt [d], M.E. Contreras-García [a]

[a] Instituto de Investigaciones Metalúrgicas y Materiales, UMSNH, Edificio U, Ciudad Universitaria, Santiago Tapia 403, Colonia Centro, 58030 Morelia, Mexico
[b] Instituto de Física, UNAM, Circuito de la Investigación s/n, Ciudad Universitaria, 04510 Coyoacán, México, D.F., Mexico
[c] Centro Multidisciplinario de Estudios en Biotecnología (CMEB) de la FMVZ, UMSNH, Posta Zootécnica, km. 8.5 carretera Morelia-Zinapecuaro, C.P. 58890 col. La Palma, Tarimbaro, Michoacán, Mexico
[d] Instituto de Investigaciones en Materiales, UNAM, Ciudad de México C.P. 04510, Mexico

ARTICLE INFO

Article history:
Received 31 October 2016
Accepted 11 February 2017
Available online 15 February 2017

Keywords:
Barium hexaferrite
Porous spherical aggregates
Surfactant-assisted sol-gel synthesis
Morphological properties
Magnetic properties

ABSTRACT

Porous spherical aggregates of barium hexaferrite ($BaFe_{12}O_{19}$) with 1.5 μm in diameter were synthetized by the surfactant-assisted sol-gel method. The surfactant Tween20 ($C_{58}H_{114}O_{26}$), which enables mesoporous structures, as well as polystyrene spheres (PS), as the template agent for the formation of macropores, were used. Two synthetic routes (hereafter named A and B), whose difference was the absence or presence of PS, were followed for synthesis. X-ray diffraction (XRD), scanning electron microscopy (SEM) and transmission electron microscopy (TEM) in high resolution mode (HRTEM) were used for characterization. Size and morphology of the spheres were similar in both cases and they resemble a nest or ball-of-yarn type structure. Pore size and $BaFe_{12}O_{19}$ crystal size produced by the two routes are different. The magnetic properties of the spheres were evaluated using a vibrating sample magnetometer (VSM) as function of the calcination temperature. The spheres present ferromagnetic behavior in both routes.

1. Introduction

In recent decades, ceramic materials represent a prominent alternative in scientific and technological development in a wide range of research fields. Specifically, biomedical ceramic materials have been used in orthopedic applications, dental implants, tissue regeneration and as drug delivery systems [1]. Iron-oxide-based materials, including barium hexaferrite ($BaFe_{12}O_{19}$), are good drug delivery system (DDS) candidates [2–4] because of their physical, chemical and magnetic properties. These magnetic properties are highly necessary for response to an external magnetic field to target, for example, the drug into a specific site in the human body. Moreover, the $BaFe_{12}O_{19}$ magnetic microparticles with spherical morphology have different applications, such as permanent magnets [5], electronic devices [6], gas sensors [7], catalytic supports [8] and more recently in biomedical applications, such as advanced functional magnetic materials for the treatment of cancer through magnetic hyperthermia [9], contrast agents for MRI [10] and drug delivery systems [11].

A variety of methods have been used for the synthesis of iron-oxide-based bioceramics including co-precipitation, hydrolysis, hydrothermal synthesis, inverse microemulsion and the sol-gel method [12–14]. Of these methods, sol-gel has attracted special interest because it allows the development of new materials with good homogeneity and purity [15–17]. In addition, it is a relatively fast, simple and inexpensive method. Moreover, the kinetics of the chemical reactions carried out in the synthesis is easily controlled by low temperatures processing [17]. Unlike classical methods for powder ceramic processing of $BaFe_{12}O_{19}$ that require high calcination temperatures (1200–1300 °C), sol-gel produces the $BaFe_{12}O_{19}$ microparticles at rather low calcination temperature [18]. In addition, the use of surfactant-assisted sol gel synthesis allows more disperse systems, enabling the formation of a larger number of ordered structures and the surfactant allows the formation of micelles that also act as templates, resulting in the formation of mesopores after elimination of the surfactant by calcination during the thermal treatment.

Surfactant-assisted sol-gel synthesis, as structure-directing agents or dispersants, and templates, as macropore-forming agents, is investigated in this work for the production of ceramic microstructures designed with hierarchical porosity for biomedical applications that require highly specific surface areas and the unique design of materials capable of conducting fluids and

* Corresponding author.
E-mail addresses: storres_c@hotmail.com (S. Torres-Cadenas), jreyes@fisica.unam.mx (J. Reyes-Gasga), brapal@hotmail.com (A. Bravo-Patiño), israelb@iim.unam.mx (I. Betancourt), eucontre@gmail.com (M.E. Contreras-García).

http://dx.doi.org/10.1016/j.jmmm.2017.02.018
0304-8853/

interacting with cell tissues. Among the materials designed for these applications, pore size distribution and their interconnectivity determine the viability of the material for a such specific application.

Therefore, in the present study $BaFe_{12}O_{19}$ spherical magnetic macro- and meso-porous microparticles were synthetized by the surfactant-assisted sol-gel method, as well as polystyrene spheres (PS) as templates for formation microspheres, and dried by spray drying. The morphological characterization and magnetic properties of the spheres are compared as a function of thermal treatment temperature.

2. Materials, method and experimental procedure

2.1. Materials

Commercial reagent grade products were used without purification. The reagents were from Aldrich: iron nitrate (III) nonahydrate $Fe(NO_3)_3{\cdot}9H_2O$, barium carbonate $BaCO_3$, and surfactant Tween20, and from Merck: ammonium hydroxide NH_4OH. The hydrophilic nonionic surfactant Tween20 ($C_{58}H_{114}O_{26}$) is an ester of polyoxyethylene sorbitan, with a molecular weight of 1225 Daltons calculated assuming 20 units of ethylene oxide, 1 sorbitol, and lauric acid as the primary fatty acid. Monodisperse Polystyrene microspheres (PS) synthesized in the laboratory were used as the pore-forming agent.

2.2. Synthesis of $BaFe_{12}O_{19}$

Spheres of barium hexaferrite were synthesized by the sol-gel method either assisted by surfactants (route A) or assisted by surfactants and templates (route B). Fig. 1 shows the flow diagram of routes A and B. Two suspensions were prepared in each route. The first was composed of $Fe(NO_3)_3{\cdot}9H_2O$ and $BaCO_3$ salts with a stoichiometric molar ratio dissolved in deionized water. The second was formed by the surfactant Tween20 in aqueous solution. Both suspensions were mixed with constant magnetic stirring and, during the reaction, the pH of the slurry was adjusted to 8 with NH_4OH. Route B included a third suspension consisting of 30 wt% polystyrene spheres in deionized water. The PS were monodispersed, with a mean diameter of 200 nm. The PS suspension was added to the mixture with constant magnetic stirring for 1 h.

The resulting suspension was subjected to spray drying, using a Mini Spray Dryer (Yamato, ADL31). The conditions in the spray drying equipment for both routes were determined by experimental design as: drying temperature (T = 175 °C) and drying pressure (P = 1.5 kg/cm^2).

Powders obtained after spray drying (xerogels) were subjected to thermal treatment for the elimination of organic agents, surfactant and template (in each case), structural water, the formation of oxides and crystallization. Four different temperatures were evaluated in both routes for thermal treatment: 700, 800, 900 and 1000 °C.

2.3. Structural, morphological, chemical and magnetic characterization

Structural, chemical and morphological analysis of the spheres was performed by X-ray diffraction (XRD), scanning electron microscopy (SEM) and transmission electron microscopy (TEM) in high resolution mode (HRTEM).

Samples were analyzed by X-ray diffraction on a Bruker diffractometer model D8 Advance using Cu Kα radiation (45 kV, 30 mA) to determine the crystal structures and phases presented. Samples were scanned from 20° to 80° in 2θ and a constant step of 0.02°/seg.

For microstructural characterization of the samples, the scanning electron microscope JEOL JSM-7600F and the transmission electron microscope FEG Phillips Technai F20 were used. The SEM was coupled with energy dispersive X-ray spectroscopy equipment (EDS).

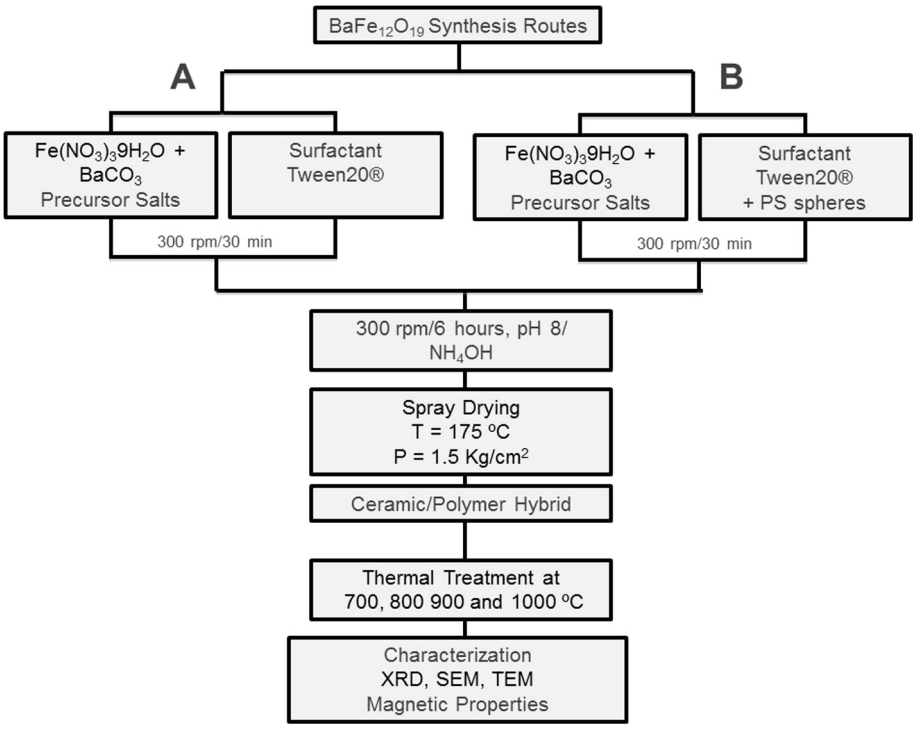

Fig. 1. Flowchart of routes A and B followed for the synthesis of the barium hexaferrite spheres. The main difference between the routes is that in route B the polystyrene spheres (PS) were added for generating macropores.

The Digital Micrograph software (Gatan, Inc.) was used for image analysis, and the linear Lynx software (Verfügbare Software) was used for the statistical analysis of the data. Size distribution of the pores in the spherical aggregates was measured by the Barrett-Joyner-Halenda (BJH) technique using a Quantachrome (St 1 on NOVA touch 1LX) instrument.

The analysis of the magnetic properties of the samples was performed using a vibrating sample magnetometer (VSM LDJ 9600) at room temperature, applying a constant magnetic field of 5000 Oe. Magnetic saturation (M_s), remanence magnetization (M_r) and coercivity (H_c) values were obtained from the hysteresis curves.

3. Results

3.1. X-ray diffraction

Fig. 2 shows the X-ray diffraction spectra of the samples obtained from routes A and B at the calcination temperatures of 700, 800, 900 and 1000 °C, as indicated in Fig. 1.

Indexing the X-ray spectra indicates the coexistence of hexaferrite H = $BaFe_{12}O_{19}$, monoferrite O = $BaFe_2O_4$ and hematite F = Fe_2O_3 in all samples. The phase H (hexaferrite) is hexagonal (Open Database Crystallography card, COD, No. 1008841) with lattice parameters a = b = 0.589 nm and c = 2.318 nm. The O (monoferrite) phase is orthorhombic (COD card No. 4107896) with lattice parameters a = 1.899 nm, b = 0.538 nm, c = 0.844 nm. The F (hematite) phase is hexagonal (COD card No. 9015964) with lattice parameters a = b = 0.503 nm and c = 1.374 nm. It is noteworthy that at the calcination temperature of 1000 °C the major phase is H phase, in both routes.

As shown in Fig. 2, the content of the H phase increases as the content of the F phase decreases with temperature in both routes. In route A, the O phase is present in all samples; in route B, the O occurs phase only in the sample treated at 700 °C. However, there is no clear evidence of preferential growth direction of any phase in the XRD spectra.

3.2. SEM images, EDS spectra and spheres and pores size

SEM images indicate that all the samples obtained in routes A and B, calcined at different temperatures, are spherical and substantially the same size. Fig. 3 shows the SEM image of the spheres obtained in route A and the insert, which shows a magnification of these spheres, indicates that the spheres are polycrystalline composed of mesopores and elongated nanometric crystals. Fig. 4 shows the SEM image of the spheres obtained through route B and the insert shows that these spheres are also polycrystalline, composed of meso- and macro-pores and micrometric elongated crystals.

Fig. 5 shows the size distribution of the spheres observed in the samples of routes A (Fig. 5A and B) thermally treated at 700 °C, respectively. Although the average size is slightly different for the samples calcined at different temperatures, all these values are within the range indicated by the standard deviation, at about 1.5 microns. Therefore, all the spherical aggregates are practically the same size. The aggregate size is the result of the droplet size produced in the nozzle of the spray dryer, although the size can also be influenced by the rheology of the gel slurry fed to the spray dryer.

Fig. 6 shows the size distribution of the pores in the spherical aggregates of routes A and B. For the mesoporous range, as mentioned above, this size distribution was measured by the BJH technique. In Fig. 6A, for the samples of route A, the average diameter of the pores in these samples are on the order of 5.7 ± 2 nm. Fig. 6B shows the case of the mesopores observed in the spheres obtained by route B; they are on the order of 12 ± 5.5 nm. The macropores in the spheres of route B have an average size of about

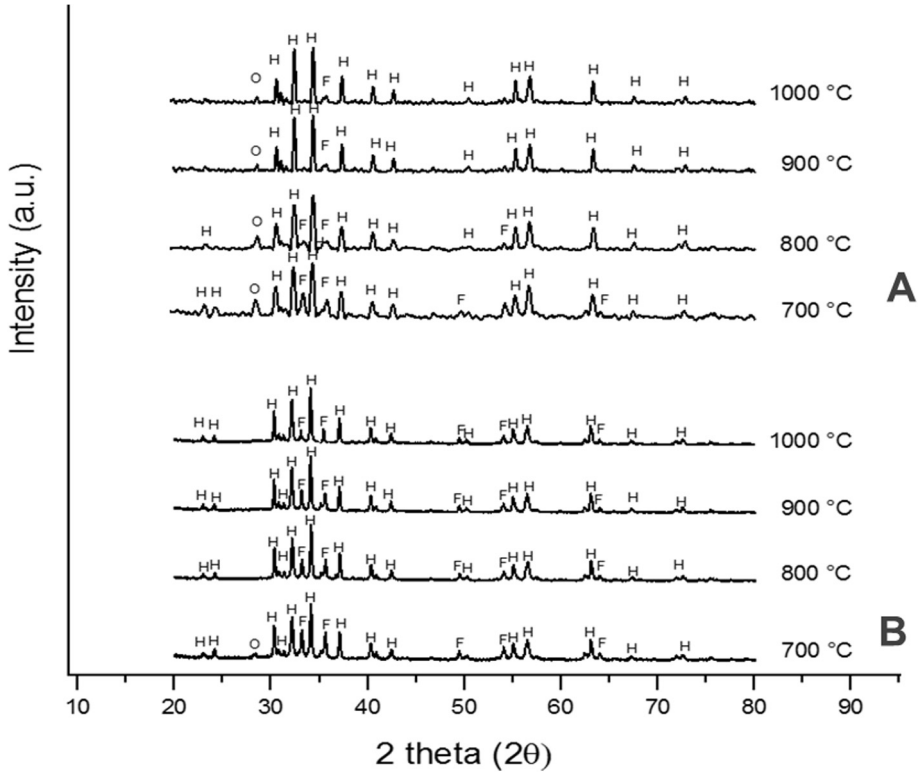

Fig. 2. XRD spectra of the samples obtained by the route A (A) and the route B (B) at the indicated calcination temperature. H = $BaFe_{12}O_{19}$, O = $BaFe_2O_4$, F = Fe_2O_3. Note that at 1000 °C the phase H is the major both cases.

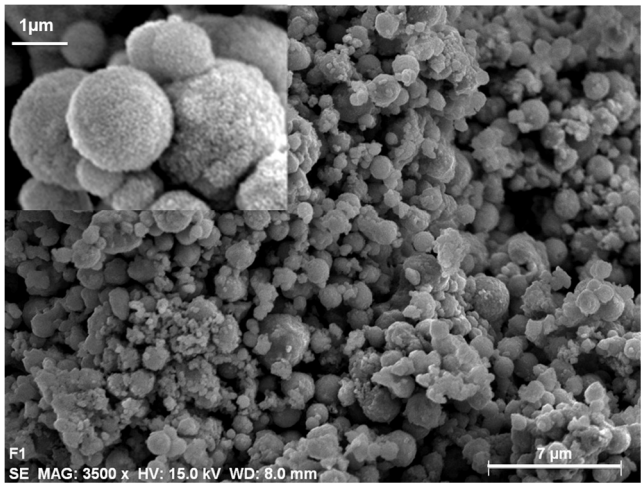

Fig. 3. SEM image of the spheres obtained in the synthesis route A. The spheres are polycrystalline, consisting of elongated crystals and nano-sized mesopores. The insert shows a magnified view.

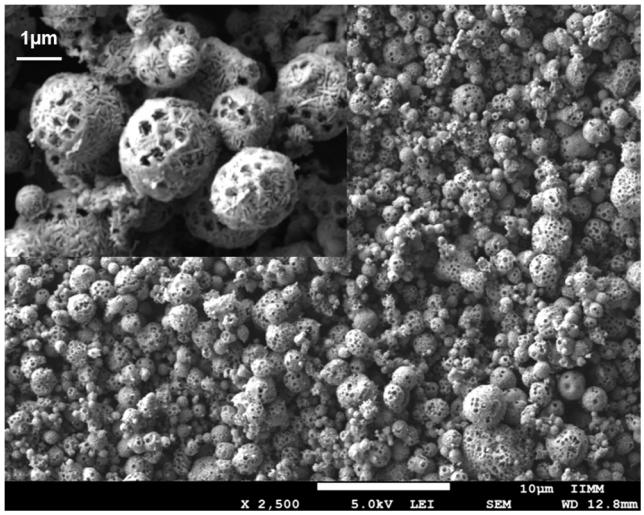

Fig. 4. SEM image of the spheres obtained in the synthesis route B. The spheres are polycrystalline with elongated crystals of micrometer size and with meso- and macro-mesoporous structure. The insert shows a magnified view.

220 ± 53 nm (Fig. 6C). This last result is logical because the suspension fed in route B consists of spheres of monomodal polystyrene whose average size is of about 250 nm, in addition to the gel.

The micrometric-size spheres obtained by route A and route B are both composed of elongated crystals, or fibers, but these crystals are of nanometric size for route A, while they are of 35 ± 7 nm wide and 300 ± 80 nm long for route B. The existence of an interconnected hierarchical pore structure in these spheres is evident.

EDS spectra from the spheres showed the characteristic peaks of barium (Ba), iron (Fe) and oxygen (O) (Fig. 7) [19]. In these spectra, the Cu peak comes from the sample holder. Therefore, the composition of spheres obtained by both routes contains the same elements, as already shown by XRD. This results also confirm that no contamination was present in either route.

3.3. TEM images

Fig. 8 shows some of the HRTEM images of the elongated crystals which conform the spheres obtained in routes A and B. Note the nanometric size of the elongated crystals of $BaFe_{12}O_{19}$. In some cases, the coexistence of crystals of $BaFe_{12}O_{19}$ with crystals of $BaFe_2O_4$ and Fe_2O_3 were observed. These images agree quite well with the results obtained by XRD and show the coexistence of a mixture of phases in the synthesized spheres in both routes.

3.4. Hysteresis loops and magnetic properties

One way to measure the magnetic properties is through the hysteresis loops, which affords the evaluation of macroscopic properties such as saturation magnetization, M_s, remanence magnetization, M_r, and coercive field. These properties define the soft or hard magnetic character of the synthesized materials. Fig. 9 shows the hysteresis loops at different calcination temperatures for the samples obtained by the route A (Fig. 9A) and the route B (Fig. 9B). The highest magnetization values are observed in the case of route B. Table 1 shows the magnetic properties of all the samples. In general, M_s, M_r and H_c show an increment as a function of the calcination temperature, and coercivity (H_c) increases with temperature in all the samples. The lowest value of M_r is obtained in the sample treated at 800 °C for route A. In route B, the lowest M_r value is obtained for the sample treated at 700 °C. There is also a clear change in the magnetic behavior associated with the temperatures of the calcination treatment. This change must be related to the percentage of content of the different phases presented in the samples, and it must also be related to the size of the crystals constituting the spherical aggregates.

From Fig. 9A and based on the values of coercivity shown in Table 1, the samples obtained in the route A at temperatures of 700, 800 and 900 °C behave as semi-hard magnetic materials, whereas the one obtained at 1000 °C behaves as a hard magnetic material. The shape of the hysteresis loop in the sample at 900 °C is characteristic of a sample in which two phases coexist. On the other hand, Fig. 9B indicates that only the material obtained at 700 °C through route B behaves as a semi-hard magnetic material; the others show hard magnetic material behavior. The semi-hard ferromagnetic behavior in these materials makes them good candidates for biomedical applications [20].

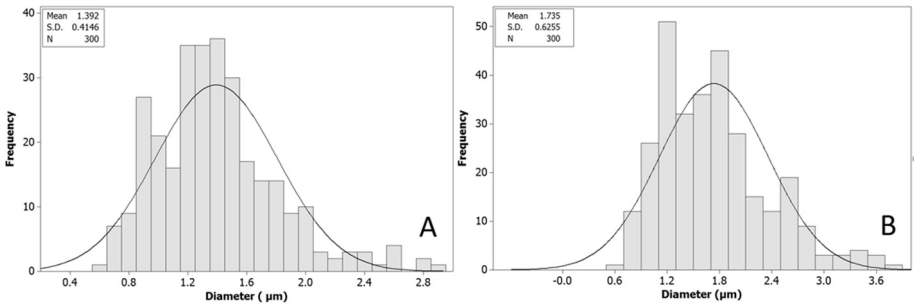

Fig. 5. A) Size distribution of the spheres in samples of route A. B) Size distribution of the spheres in samples of route B.

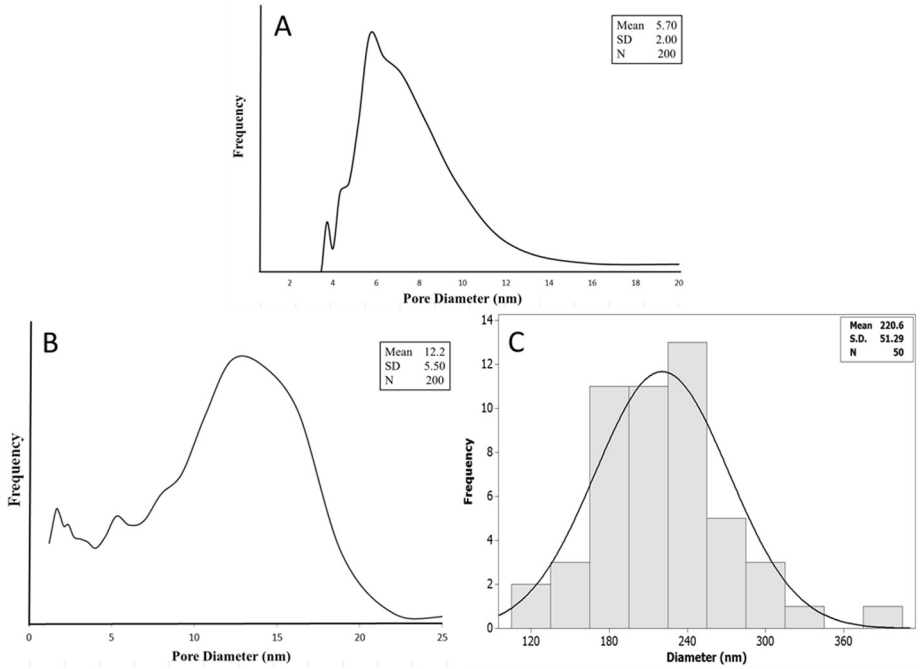

Fig. 6. Size distribution of the mesopores of the spheres measured by the BJH technique. A) Route A: 5.7 ± 2 nm. B) Route B: 12 ± 5.5 nm. C) Size distribution of the macropores in the spheres of route B: on average they are on the order of 220 ± 53 nm.

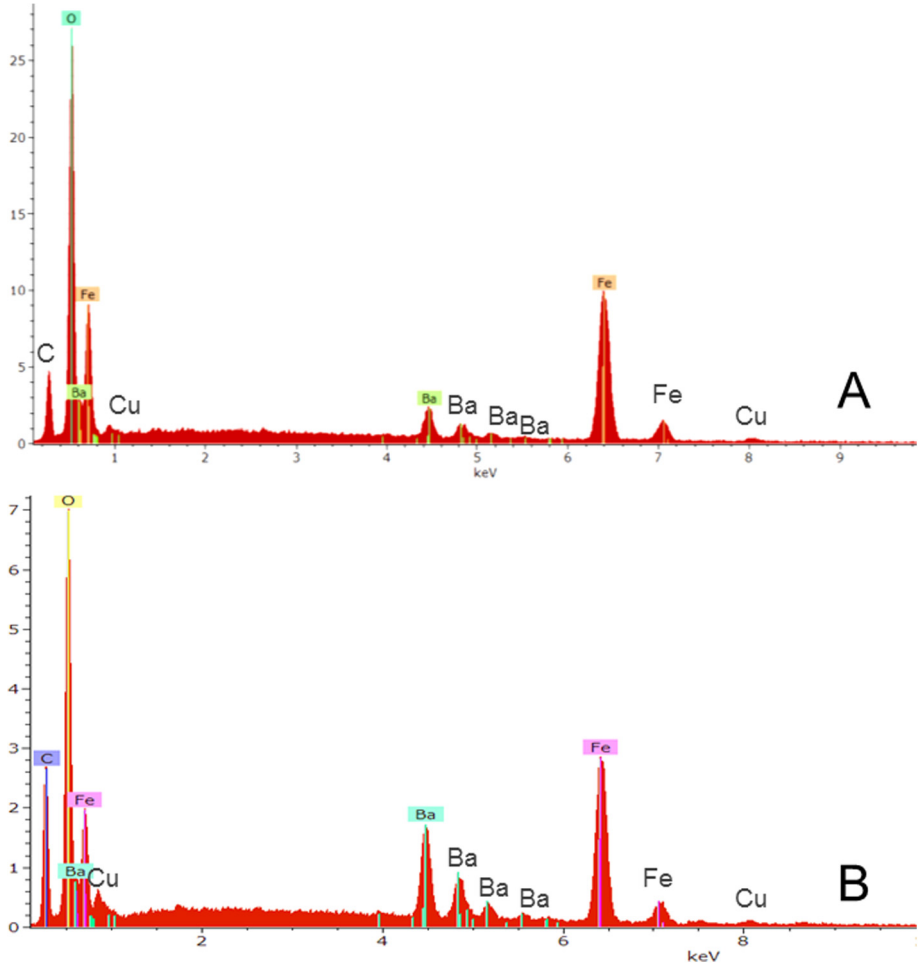

Fig. 7. EDS spectra of the spheres obtained in the route A (A) and in the route B (B). The spectra are similar for both routes and correspond to the elements Ba, Fe and O.

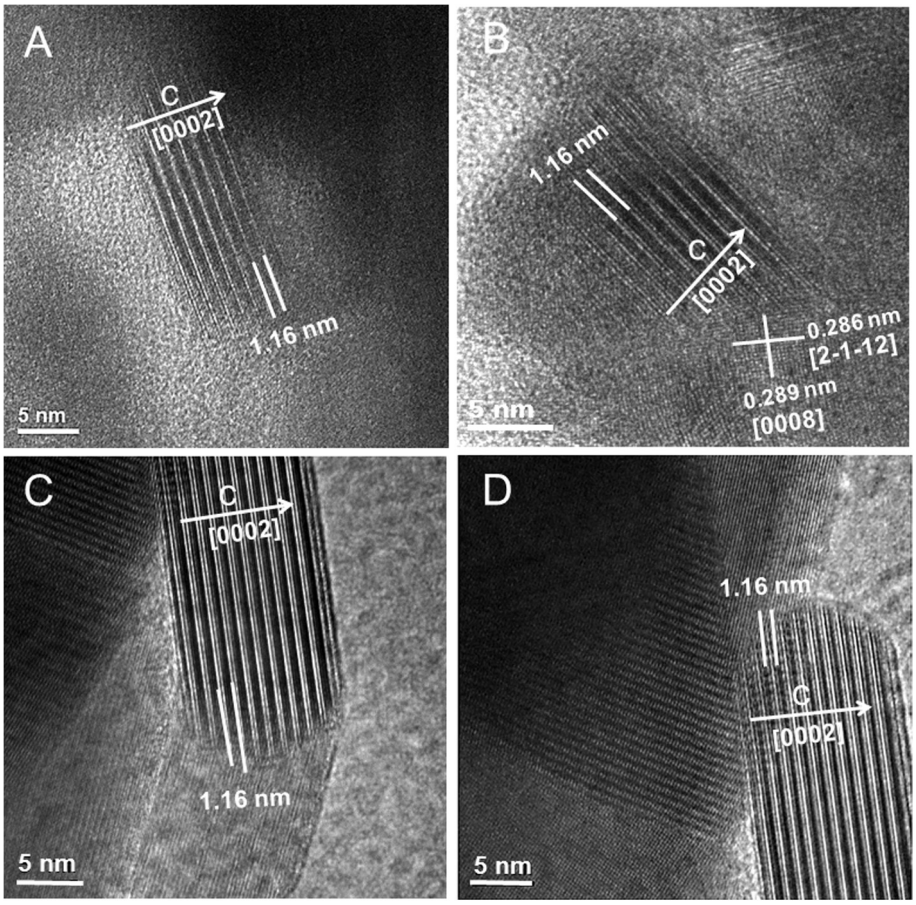

Fig. 8. HRTEM images of the crystals of $BaFe_{12}O_{19}$ that make up the spheres obtained in the routes A (A–B) and B (C–D).

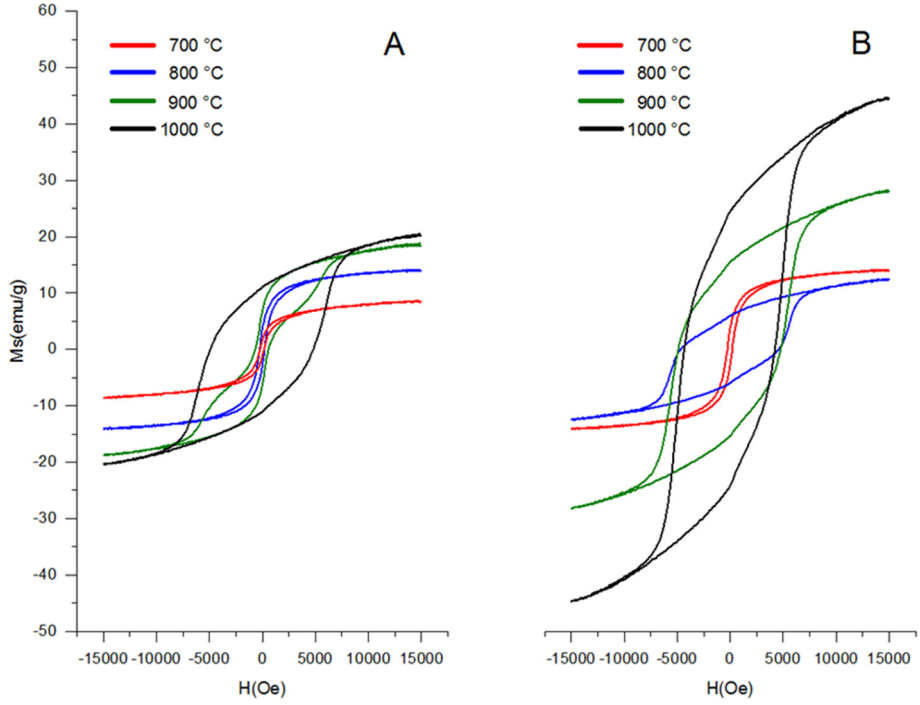

Fig. 9. Hysteresis loops registered in the samples obtained by route A (A) and route B (B) at different calcination temperatures. Note the difference in the magnetic behavior between the two routes in relation to the calcination temperature, reaching higher magnetization values in the case of route B.

Table 1
Magnetic properties of the samples calcined at different temperatures according to route A (A) and route B (B). The values were obtained from the hysteresis loops shown in Fig. 9.

Magnetic properties				
Route	Calcination temperature (°C)	M_s (emu/g)	M_r (emu/g)	H_c (Oe)
A	700	24.61	5.93	242.20
	800	17.28	2.73	234.51
	900	23.71	9.10	667.40
	1000	44.67	24.12	4790.12
B	700	14.24	3.79	194.65
	800	12.49	5.92	4631.60
	900	28.26	15.27	4791.46
	1000	45.11	24.10	4277.50

4. Discussion

The results clearly indicate that we succeed in developing a route for the synthesis of porous spheres of barium hexaferrite with different pore sizes. The porous structures are of great interest in research because of their prominent applications in different fields of science [21]. For example, they can be used to charge an adequate amount of different types of molecules (i.e. drugs, proteins and/or peptides) within the interior of the pore (and also on the surface of the structure) thus acting as a drug carrier system [22]. Mesopores are useful in applications where interaction with fluids is part of the integration process in which molecules will be exchanged in the system, as in the case of drug delivery. Macropores allow the adsorption of large molecules, such as proteins or peptides, or even cells that are currently of great interest in the development of new medical treatments based on the 'in situ' drug delivery such as magnetofection [23], gene therapy [24] and cell labeling [25].

In obtaining macropores, the surface charge of the PS spheres and steric factors play an important role in the self-assembly of $BaFe_{12}O_{19}$ precursor ions into the PS particles [26]. Pores in the spherical aggregates are consequently produced when the system is subjected to thermal treatment (700, 800, 900 and 1000 °C) resulting in the pyrolysis of the surfactant and the PS. Thus, the $BaFe_{12}O_{19}$ precursor ions are adsorbed into the PS surface, being embedded within the micrometer size spherical aggregate during the spray drying. This reaction can be considered a typical polymerization reaction, which means that polymerization takes place between $BaFe_{12}O_{19}$ and PS particles contained in an aqueous phase [27]. As a result, the PS/$BaFe_{12}O_{19}$ hybrid particles are obtained.

In regard to magnetic behavior, the hysteresis loops indicate that materials produced at temperatures of 700, 800 and 900 °C in route A fall within the range of semi-hard magnetic materials, whereas at 1000 °C the material becomes a hard magnetic material. In the case of route B, the material behaves like a semi-hard magnetic material only at 700 °C. The obtained materials behave like hard magnetic materials from 800 °C to 1000 °C. Analysis of the structural composition of the spheres indicated that monoferrite (O) and hematite (F) phases are present. However, the H phase is the major phase at the calcination temperature of 1000 °C.

As shown in Table 1, a significant change occurred as function of calcination temperature in the magnetic properties of the samples. This change has also to be related to the presence of the different phases. Best combinations of magnetic properties were: M_s = 44.67 emu/g and H_c = 4790.12 Oe for route A; and M_s = 45.11 emu/g and H_c = 4791.46 Oe for route B, respectively.

The coexistence of the H, O and F phases has been reported as a general fact in obtaining barium hexaferrite [28]. The O phase presents an anomalous resonance near 400 °C that could indicate a phase with magnetic behavior [29]. The F phase has anti-ferromagnetic ordering [30], and thus, a characteristic low M_s (11.05 emu/g) [31–33]. Therefore, for route B, it is possible to attribute the observed M_s variations to the variable content of this phase, so that, the sample with greater amount of Fe_2O_3 (at 700 °C) presents a very low value of M_s. Decreasing presence of Fe_2O_3 (by progressively increasing the temperature), increases the proportion of the hexaferrite phase and consequently, the M_s values are significantly recovered. In route A, the larger value of M_s is coupled with a larger value of H_c, which must be attributed to the presence of a large amount of hexaferrite phase. By contrast, in the route B, the largest value of M_s of the sample sintered at 1000 °C does not imply a larger value of H_c (which is recorded for the sample sintered at 900 °C), which is most like due to significance differences in particle size between the two phases Samples with H_c > 4000 Oe can be considered as materials with hard magnetic behavior.

Therefore, it seems in this study, a larger amount of the Fe_2O_3 phase obtained at lower temperatures contributes to a decrement in the magnetic properties, resulting in semi-hard magnetic behavior, while an increment in hard magnetic behavior can mainly be attributed to a decrement in the amount of the Fe_2O_3 phase, as the $BaFe_{12}O_{19}$ phase increases.

5. Conclusions

Porous spherical aggregates of barium hexaferrite ($BaFe_{12}O_{19}$) of approximately 1.5 μm in diameter and 200 nm pores were obtained by the sol-gel chemical synthesis method using polystyrene (PS) as the pore-forming agent. The morphology of the spheres resembles a nest or ball-of-yarn type structure in which the crystals belong to the barium hexaferrite phase, as the major phase, in coexistence with the monoferrite ($BaFe_2O_4$) and hematite (Fe_2O_3) phases. However, the barium hexaferrite phase is the major phase at the calcination temperature of 1000 °C. The magnetic properties of the spheres indicate that the samples calcined at 700 °C present semi-hard magnetic behavior, suggesting they would be good candidates for use in biomedical applications.

Acknowledgements

We thank to V. S. López Alvarez and A. Rodriguez Torres for the technical support. STC acknowledges the Consejo Nacional de Ciencia y Tecnología (CONACYT) by scholarship and CIC-UMSNH for the financial support to this research.

References

[1] J. Chevalier, L. Gremillard, Ceramics for medical applications: a picture for the next 20 years, J. Eur. Ceram. Soc. 29 (2009) 1245–1255.
[2] C. Oka, K. Ushimaru, N. Horiishi, T. Tsuge, Y. Kitamoto, Core–shell composite particles composed of biodegradable polymer particles and magnetic iron oxide nanoparticles for targeted drug delivery, J. Magn. Magn. Mater. 381 (2015) 278–284.
[3] S. Chandra, G. Noronha, S. Dietrich, H. Lang, D. Bahadur, Dendrimer-magnetic nanoparticles as multiple stimuli responsive and enzymatic drug delivery vehicle, J. Magn. Magn. Mater. 380 (2015) 7–12.
[4] M. Mahmoudi, S. Sant, B. Wang, S. Laurent, T. Sen, Superparamagnetic iron oxide nanoparticles (SPIONs): development, surface modification and applications in chemotherapy, Adv. Drug Delivery Rev. 63 (2011) 24–46.
[5] G.H. An, T.Y. Hwang, J. Kim, J.B. Kim, N. Kang, S. Kim, Y.M. Choi, Y.H. Choa, Barium hexaferrite nanoparticles with high magnetic properties by salt-assisted ultrasonic spray pyrolysis, J. Alloy. Compd. 583 (2014) 145–150.
[6] M. Choi, S. Cho, Y. Song, S. Baek, H. Kim, J. Jung, H. Lee, C. Park, S. Park, Y. Kim, Synthesis and characterization of hollow $BaFe_{12}O_{19}$ submicron spheres for advance functional magnetic materials, Curr. Appl. Phys. 14 (2014) 1208–1211.
[7] X. Xu, J. Park, Y.K. Hong, A.M. Lane, Ethylene glycol assisted spray pyrolysis for the synthesis of hollow $BaFe_{12}O_{19}$ spheres, Mater. Lett. 144 (2015) 119–122.
[8] P. Ren, J.G. Guan, X.D. Cheng, Influence of heat treatment conditions on the structure and magnetic properties of barium ferrite $BaFe_{12}O_{19}$ hollow microspheres of low density, Mater. Chem. Phys. 98 (2006) 90–94.
[9] X. Xu, J. Park, Y.K. Hong, A.M. Lane, Synthesis and characterization of hollow mesoporous $BaFe_{12}O_{19}$ spheres, J. Solid State Chem. 222 (2015) 84–89.

[10] L. Junliang, L. Ping, Z. Xingkai, P. Dongjun, Z. Peng, Z. Ming, Synthesis and properties of single domain sphere-shaped barium hexa-ferrite nano powders via an ultrasonic-assisted co-precipitation route, Ultrason. Sonochem. 23 (2015) 46–52.
[11] M. Choi, S. Cho, Y. Song, D. Choi, S. Park, Y. Kim, Novel synthesizing method of $BaFe_{12}O_{19}$ micro rod and its superior coercivity with shape anisotropy, Mater. Letter. 139 (2015) 292–295.
[12] G. Nabiyouni, D. Ghanbari, A. Yousofnejad, M. Seraj, A sonochemical-assisted method for synthesis of $BaFe_{12}O_{19}$ nanoparticles and hard magnetic nanocomposites, J. Ind. Eng. Chem. 20 (2014) 3425–3429.
[13] A.F. Arif, R. Balgis, T. Ogi, T. Mori, K. Okuyama, Experimental and theoretical approach to evaluation of nanostructured carbon particles derived from phenolic resin via spray pyrolysis, Chem. Eng. J. 271 (2015) 79–86.
[14] G.G. Nedelcu, A. Nastro, L. Filippelli, M. Cazacu, M. Iacob, C. Oliviero Rossi, A. Popa, D. Toloman, M. Dobromir, F. Iacomi, Structural characterization of copolymer embedded magnetic nanoparticles, Appl. Surf. Sci. 352 (2015) 109–116.
[15] J.D. Wright, N.A.J.M. Sommerdijk, Sol-Gel Materials Chemistry and Applications. Series Advanced Chemistry Texts, CRC Press, USA, New York, 2005.
[16] A.C. Pierre, Introduction to Sol-Gel Processing, Kluwer Academic Publishers, Boston/London, 2002.
[17] Z. Min-Jian, X. Guo-Ging, M. Hong-Liang, Z. Jiong, Y. Zhong-Yue, H. Zheng-Ming, Influence of citric acid content on magnetic properties of $BaFe_{12}O_{19}$ powder prepared by sol-gel auto-combustion method, J. Shanghai Univ. (English Edition) 11 (2007) 263–267.
[18] A. Ataie, A. Mali, Characteristics of barium hexaferrite nanocrystalline powders prepared by a sol-gel combustion method using inorganic agent, J. Electroceram. 21 (2008) 357–360.
[19] A. Ghasemi, R.S. Alam, A. Morisako, Preparation and magnetic properties of hexagonal barium ferrite films using BaM nanoparticles, Phys. B 403 (2008) 2987–2990.
[20] D. Niarchos, Magnetic MEMS: key issues and some applications, Sens. Actuators A 109 (2003) 166–173.
[21] A. Bayu, D. Nandiyanto, S.G. Kim, F. Iskandar, K. Okuyama, Synthesis of spherical mesoporous silica nanoparticles with nanometer-size controllable pores and outer diameters, Microporous. Mesoporous. Mater. 120 (2009) 447–453.
[22] K. Okuyana, M. Abdullah, I.W. Lenggoro, F. Iskandar, Preparation of functional nanostructured particles by spray drying, Adv. Powder Technol. 17 (2006) 587–611.
[23] C. Plank, O. Zelohati, O. Mykhaylyk, Magnetically enhanced nucleic acid delivery. Ten years of magnetofection-progress and prospect, Adv. Drug Delivery Rev. 63 (2011) 1300–1331.
[24] V.I. Shubayev, T.R. Pisanic, S. Jin, Magnetic nanoparticles for theragnostics, Adv. Drug Delivery Rev. 61 (2009) 467–477.
[25] D. Arunbabu, T. Jana, Charged polystyrene nanoparticles: role of ionic comonomers structures, J. Colloid Interface Sci. 361 (2011) 534–542.
[26] H. Zhoua, T. Shia, X. Zhoua, Preparation of polystyrene/SiO_2 microsphere via pickering emulsion polymerization: synergistic effect of SiO_2 concentrations and initiator sorts, Appl. Surf. Sci. 266 (2013) 33–38.
[27] A. Javidan, M. Ramezani, A. Sobhani-Nasab, S.M. Hosseinpour-Mashkani, J. Mater. Sci.: Mater. Electron. 26 (2015) 3813–3818.
[28] Y. Chung, S.K. Lim, C.K. Kim, Y.H. Kim, C.S. Yoon, Synthesis of γ-Fe_2O_3 nanoparticles embedded in polyimide, J. Magn. Magn. Mater. 272–276 (2004) E1167–E1168.
[29] M. Tadić, N. Čitaković, M. Panjan, Z. Stojanović, D. Marković, V. Spasojević, Synthesis, morphology, microstructure and magnetic properties of hematite submicron particles, J. Alloy. Compd. 509 (2011) 7639–7644.
[30] S. Kamali, N. Shahmiri, J.S. Garitaonandia, J. Ångström, M. Sahlberg, T. Ericsson, L. Häggström, Effect of mixing tool on magnetic properties of hematite nanoparticles prepared by sol–gel method, Thin Solid Films 534 (2013) 260–264.
[31] H. Hao, D. Sun, Y. Xu, P. Liu, G. Zhang, Y. Sun, D. Gao, Hematite nanoplates: controllable synthesis, gas sensing, photocatalytic and magnetic properties, J. Colloid Interface Sci. 462 (2016) 315–324.
[32] M. Chirita, I. Grozescu, Fe_2O_3-nanoparticles, physical properties and their photochemical and photoelectrochemical applications, Chem. Bull. "Politehnica" Univ. (Timisoara) 54 (2009) 1–8.
[33] N.A. Frey, S. Peng, K. Cheng, S. Sun, Magnetic nanoparticles: synthesis, functionalization, and applications in bioimaging and magnetic energy storage, Chem. Soc. Rev. 38 (2009) 2532–2542.